ADVANCED ENERGY MATERIALS
www.advenergymat.de

Regulating the Hidden Solvation-Ion-Exchange in Concentrated Electrolytes for Stable and Safe Lithium Metal Batteries

Rachid Amine, Jianzhao Liu, Ilona Acznik, Tian Sheng, Katarzyna Lota, Hui Sun, Cheng-Jun Sun, Krzysztof Fic, Xiaobing Zuo, Yang Ren, Deia Abd EI-Hady, Wael Alshitari, Abdullah S. Al-Bogami, Zonghai Chen, Khalil Amine, and Gui-Liang Xu**

Lithium–sulfur batteries are attractive for automobile and grid applications due to their high theoretical energy density and the abundance of sulfur. Despite the significant progress in cathode development, lithium metal degradation and the polysulfide shuttle remain two critical challenges in the practical application of Li–S batteries. Development of advanced electrolytes has become a promising strategy to simultaneously suppress lithium dendrite formation and prevent polysulfide dissolution. Here, a new class of concentrated siloxane-based electrolytes, demonstrating significantly improved performance over the widely investigated ether-based electrolytes are reported in terms of stabilizing the sulfur cathode and Li metal anode as well as minimizing flammability. Through a combination of experimental and computational investigation, it is found that siloxane solvents can effectively regulate a hidden solvation-ion-exchange process in the concentrated electrolytes that results from the interactions between cations/anions (e.g., Li^+, $TFSI^-$, and S^{2-}) and solvents. As a result, it could invoke a quasi-solid-solid lithiation and enable reversible Li plating/stripping and robust solid-electrolyte interphase chemistries. The solvation-ion-exchange process in the concentrated electrolytes is a key factor in understanding and designing electrolytes for other high-energy lithium metal batteries.

1. Introduction

The pursuit of high energy and low-cost energy storage devices to satisfy the ever-growing energy demand has resulted in the exploration of novel chemistries beyond conventional lithium-ion battery technologies. Among these, lithium–sulfur (Li–S) batteries are considered as attractive candidates for automotive and grid applications because of their high theoretical energy density (2600 Wh kg^{-1}) and the abundance of sulfur.[1] Despite the significant advances in the past decades, two major obstacles result from lithium polysulfide (LiPSs) shuttle and lithium dendrite formation, significantly imped the practical implementation of Li–S batteries.[2] The former is due to the dissolution and migration of LiPSs intermediates in conventional ether-based electrolytes, which not only cause loss of active materials, but also induce severe parasitic

R. Amine
Department of Chemical Engineering
University of Illinois at Chicago
Chicago, IL 60607, USA

R. Amine
Materials Science Division
Argonne National Laboratory
Lemont, IL 60439, USA

Dr. J. Z. Liu, Dr. Z. Chen, Dr. K. Amine, Dr. G.-L. Xu
Chemical Sciences and Engineering Division
Argonne National Laboratory
9700 S Cass Avenue, Lemont, IL 60439, USA
E-mail: amine@anl.gov; xug@anl.gov

The ORCID identification number(s) for the author(s) of this article can be found under https://doi.org/10.1002/aenm.202000901.

DOI: 10.1002/aenm.202000901

Dr. J. Liu
Department of Chemistry
Virginia Tech
900 West Campus Drive, Blacksburg, VA 24061, USA

Dr. I. Acznik, K. Lota
Institute of Non-Ferrous Metals Division in Poznan Central Laboratory of Batteries and Cells
Forteczna 12, Poznan 61-362, Poland

Dr. T. Sheng
College of Chemistry and Materials Science
Anhui Normal University
Wuhu 241000, P. R. China

Dr. H. Sun
State Key Laboratory of Heavy Oil Processing
Institute of New Energy
China University of Petroleum-Beijing
Beijing 102249, P. R. China

Dr. C.-J. Sun, Dr. X. Zuo, Dr. Y. Ren
X-ray Science Division
Argonne National Laboratory
9700 South Cass Avenue, Lemont, IL 60439, USA

reactions with the Li metal anode and result in the formation of porous or mossy Li metal after cycling.[3] The latter originates from the parasitic reactions of lithium metal with the electrolytes, leading to the formation of a fragile solid-electrolyte interphase (SEI) on the Li metal, further uncontrolled lithium dendrite growth, and eventually dead lithium.[4] These parasitic reactions are the direct cause for the rapid capacity fade and poor coulombic efficiency of Li–S batteries.

To achieve long cycle life and high coulombic efficiency in Li–S batteries, much effort has been devoted to eliminating these parasitic reactions by use of multifunctional cathodes and electrolytes.[1b,5] Inspired by the concept of sulfur confinement,[6] researchers are striving to suppress the dissolution of LiPSs by encapsulating sulfur within or onto various nanostructured host materials.[7] Despite the improved cycle stability, the encapsulated sulfur cathodes barely achieve superior coulombic efficiency (<100%) during cycling, indicating continuous occurrence of parasitic reactions inside the Li–S cells.[6,8] This problem is due to the limited accommodation sites and the weak binding strength of host materials toward LiPSs.[5a] As a result, the formed LiPSs could be readily detached from the host materials during cycling and lead to the aforementioned capacity degradation and Li corrosion. This process would further cause rapid cell failure in the practical Li–S pouch cells due to the limited amount of Li on the anode side.

On the other hand, in order to achieve high sulfur redox reaction kinetics, the conventional electrolytes for Li–S batteries are using 1.0 M lithium bis(trifluoromethanesulfonyl)imide (LiTFSI) in a mixture of low-donor-number solvents such as 1,3-dioxolane (DOL) and 1,2-dimethoxyethane (DME). However, these ether-based electrolytes have high LiPSs solubility, leading to self-discharge and shortened cycle life of Li–S batteries.[9] Moreover, despite the relatively lower reactivity with Li metal compared to organic carbonate electrolytes, these electrolytes cannot sustain durable lithium plating/stripping during prolonged cycling.[10] In addition, they are highly volatile and have a very low flash point (<2 °C), posing severe safety risks for batteries when operating at elevated temperatures.[11] An alternative approach is to use high-donor-number solvents, such as dimethylacetamide and dimethylsulfoxide, which can increase the sulfur utilization and tailor the deposition morphology of Li_2S.[12] However, these electrolytes suffer from the formidable drawback of high reactivity with Li metal.[13] Therefore, optimal electrolytes that can overcome these shortcoming for Li–S batteries are needed.

Dr. K. Fic
Poznan University of Technology
Pl. Marii Sklodowskiej-Curie 5, Poznan 60-965, Poland
Dr. D. A. EI-Hady, W. Alshitari, A. S. Al-Bogami
Department of Chemistry
College of Science
University of Jeddah
P.O. 80327, Jeddah 21589, Saudi Arabia
Dr. K. Amine
Materials Science and Engineering
Stanford University
Stanford, CA 94305, USA
Dr. K. Amine
IRMC
Imam Abdulrahman Bin Faisal University (IAU)
Dammam 34212, Saudi Arabia

Concentrated electrolytes have been recently considered as an appealing solution for the development of long-life lithium metal batteries.[14] This is because of their numerous physical/electrochemical merits over the traditional dilute electrolytes (<1.2 M), such as better reductive/oxidative stability, lower flammability, lower volatility, higher Li^+ transport number, and a salt-derived SEI.[15] A pioneering work by Suo et al. showed that a solvent-in-salt electrolyte with ultrahigh salt concentration (up to 7.0 M) can suppress LiPSs dissolution and lithium dendrite growth simultaneously due to the scarcity of free solvents in the electrolytes, leading to significantly improved cycle stability and coulombic efficiency.[16] However, the encapsulated sulfur cathodes still undergo a two-step solid–liquid–solid lithiation process in these concentrated electrolytes, indicating the formation of LiPSs intermediates. As the dissolution of LiPSs relies on the solvation with the solvents, a question remaining here is: where do the free solvents come from since almost all the solvent molecules should have been well coordinated by the cations/anions of lithium salts in the super-concentrated electrolytes? A fact that has been ignored for a long time is the solvating power difference among various cations/anions (e.g., Li^+, $TFSI^-$, and S_x^{2-}) with the solvents, which could initiate a solvation-ion-exchange (SIE, expressed as $TFSI^-_{(sol)} + Li_2S_x \rightarrow S_x^{2-}{}_{(sol)} + LiTFSI_{(sol)}$) process and hence result in the solvation and re-formation of soluble LiPSs during cycling.

In this work, through experimental and computational studies, we have identified an unprecedented correlation between parasitic reactions and the SIE process in Li–S batteries. For the first time, we report a new class of concentrated siloxane-based electrolytes for Li–S batteries, which demonstrated significant advantages over the widely deployed ether-based electrolytes (both dilute and concentrated). The siloxane electrolytes can effectively eliminate the hidden SIE process and can thereby simultaneously limit the dissolution of LiPSs and lithium dendrite growth. Therefore, we can enable zero parasitic reactions in Li–S batteries, corresponding to 100% coulombic efficiency, even for nonencapsulated sulfur cathodes. In addition, because of the high flash point of siloxane solvents (>70 °C), the concentrated siloxane electrolytes are intrinsically nonflammable. The insights in this work could provide a new route for developing stable and safe lithium metal batteries with high coulombic efficiency.

2. Results and Discussion

2.1. Solvation-Ion-Exchange Process in Li–S Batteries

To reveal the critical role of solvation and ion exchange in Li–S batteries, two widely investigated ether-based electrolytes have been selected for comparison in this work. They are based on conventional dilute (typical 1.0 M) ether and concentrated (5.0 M) ether (DOL/DME) (see the Experimental Section for details). **Scheme 1**a shows the schematic structures of the most common species in the electrolytes, including free solvent molecules, solvent-separated ion pairs (SSIPs), contact ion pairs (CIPs), and cation–anion aggregates (AGGs). In the dilute ether electrolytes, Li^+ is normally coordinated with four solvent molecules, which is much lower than the solvent/Li salt molar ratio and hence results in a considerable amount of free solvent molecules. As shown in Scheme 1b,

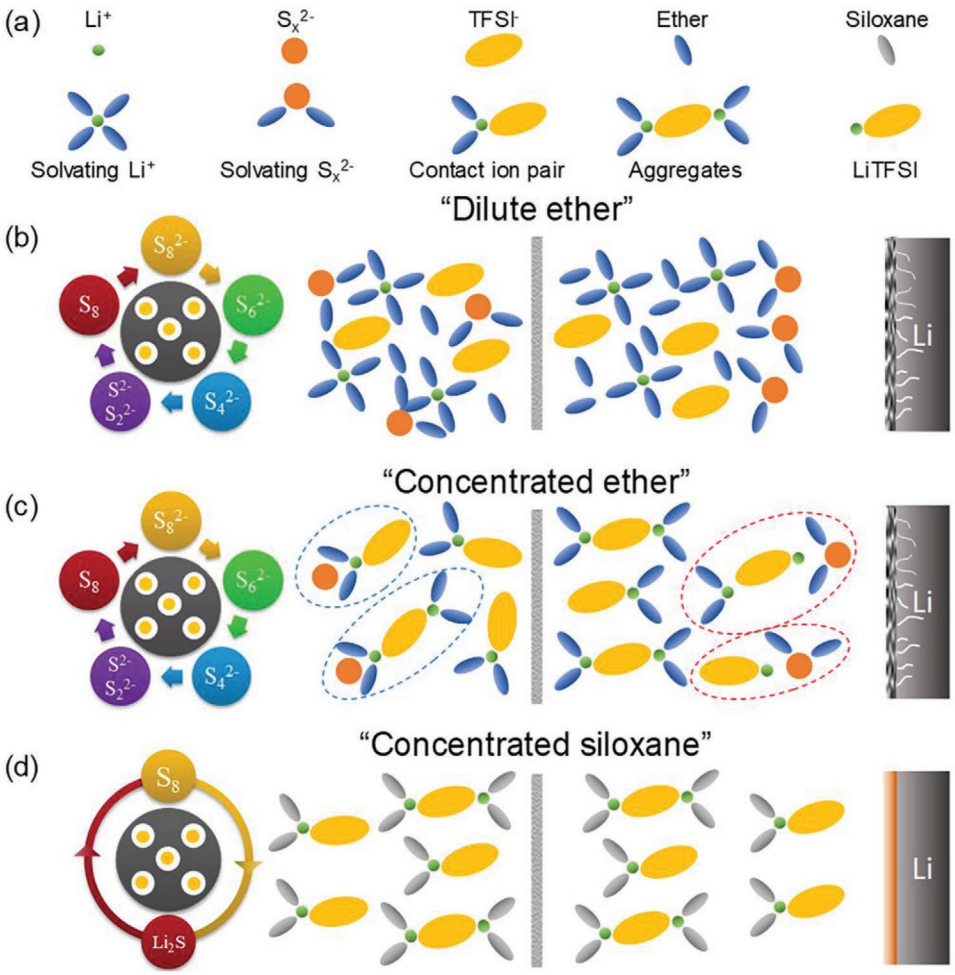

Scheme 1. Schematic illustration of sulfur redox chemistry, polysulfide shuttle, and lithium dendrite formation for Li–S batteries in different electrolytes: a) common species in the electrolytes and b) dilute ether, c) concentrated ether, and d) concentrated siloxane electrolytes.

these molecules very easily either solvate with S_x^{2-} or react with Li metal, leading to a two-step solid–liquid–solid lithiation pathway and Li dendrite formation. With increased Li salt concentration, the amount of free solvents is significantly decreased, and the Li salt tends to form CIPs and AGGs rather than SSIPs. At a very high concentration (e.g., 7.0 M), almost all the solvent molecules are in Li^+-solvating states, and there are no free solvent molecules in the electrolytes. However, as shown in Scheme 1c, the solvating power difference between $TFSI^-$ and S_x^{2-} with the ether solvent molecules can result in SIE and re-formation of solvated S_x^{2-}, as marked by the dashed blue and red circles. Therefore, the encapsulated sulfur cathodes still present two-step solid–liquid–solid transformation, and the solvated S_x^{2-} would still cause corrosion of Li metal and alter Li stripping/plating behavior. Ideally, an optimal electrolyte would have strong solvation with cations/anions in the lithium salts but relatively weak solvation with polysulfides. In light of these two requirements, we report a new class of concentrated siloxane-based electrolyte that can regulate the hidden SIE, leading to one-step solid–solid lithiation and stable lithium stripping/plating during charge/discharge, as illustrated in Scheme 1d. The structures and basic properties of siloxanes can be found in Figure S1 and Table S1 (Supporting Information).

The solvation chemistries of the concentrated siloxane electrolytes were investigated by Raman, small-angle X-ray scattering (SAXS), and ab initio molecular dynamics (AIMD) studies. As shown in **Figure 1**a, the pure siloxane solvent exhibits two O–Si $(CH_3)_3$ vibration bands at 608 and 613 cm^{-1}. These band shifts up to ≈620 cm^{-1} when the siloxane participates in Li^+ solvation. As the LiTFSI concentration increases, the fraction of free siloxane solvents decreases, and that of Li^+-coordinated siloxane substantially increases. Meanwhile, the Li^+-$TFSI^-$ association simultaneously intensifies through the formation of CIP and AGG clusters, as evidenced from a remarkable upshift of the $TFSI^-$ band (730–760 cm^{-1}, Figure 1b). At a high concentration of 5.0 M, almost all the free siloxane molecules are solvating to Li^+ and $TFSI^-$. This finding is further confirmed by the AIMD simulation, which provides an atomic-scale understanding on the solvation structure around the Li^+ cations (Figure 1c,d, as well as Figure S2, Supporting Information). With increasing LiTFSI concentration, the portion of coordinated Li^+ significantly increases (Figure 1e), while the proportions of the free DOL and siloxane molecules

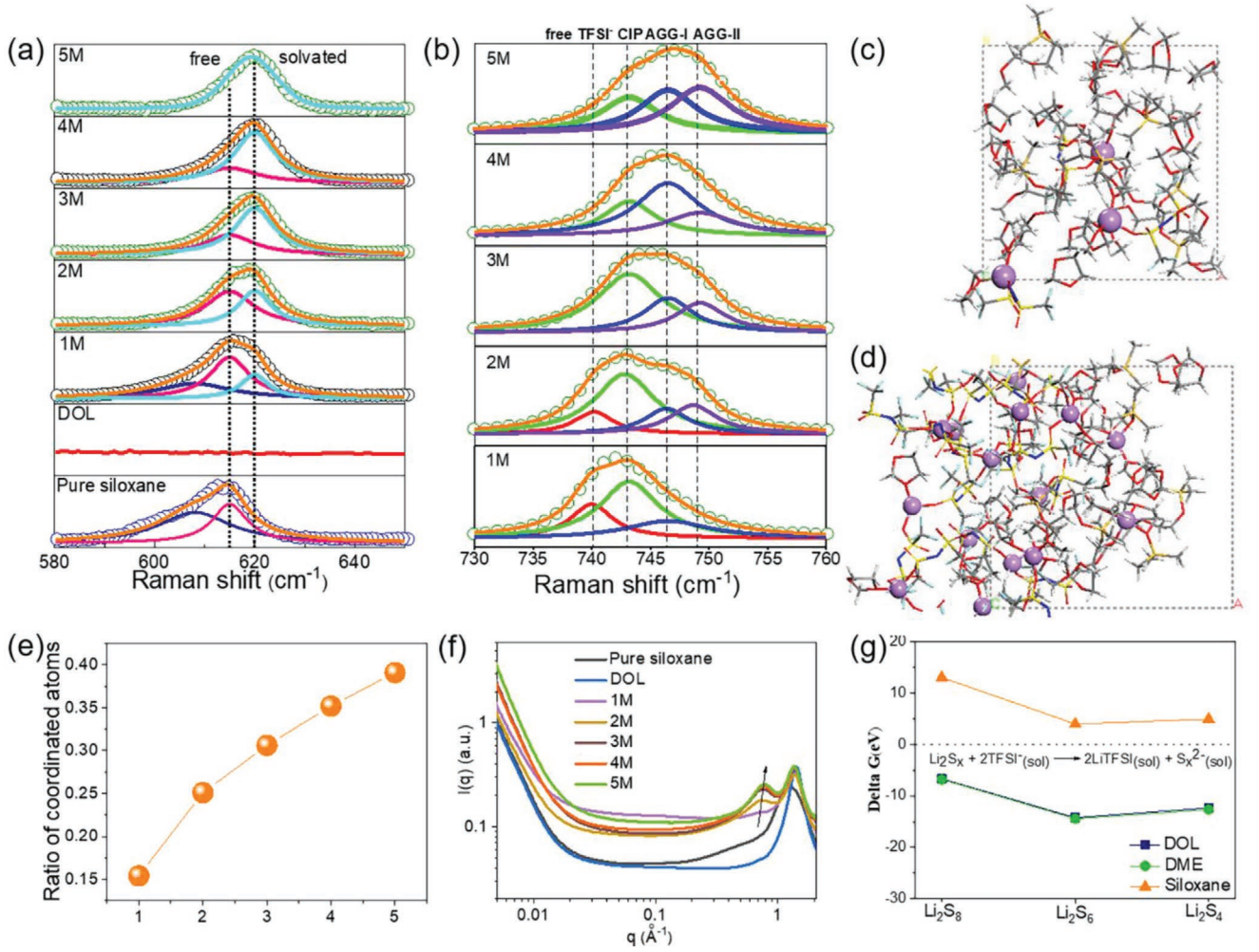

Figure 1. Raman spectra of siloxane electrolytes with different concentrations in the range of a) 580–650 cm^{-1} and b) 730–760 cm^{-1}. Snapshots of the AIMD optimized structures of c) 1.0 M and d) 5.0 M siloxane electrolytes. e) Percentage of coordinated Li^+ with increasing LiTFSI concentration in concentrated siloxane electrolytes. f) SAXS data of siloxane-based electrolytes with increased LiTFSI concentration. g) Calculated SIE energy of polysulfides with different solvents determined by Gaussian simulation. The white, grey, red, purple, cyan, yellow and blue atoms represent H, C, O, Li, F, S, and N, respectively.

in the electrolytes are greatly reduced accordingly (Figure S3, Supporting Information). A careful comparison on the local structure of Li^+ cations in the 1.0 and 5.0 M electrolytes clearly showed a transition from four to three coordination (Figures S4 and S5, Supporting Information).

The interactions between cations/anions and electrolyte solvents were further investigated by SAXS, which has been proved to be a very powerful technique for studying solution structures and the nanostructures present in electrolyte systems and can detect clusters with a size of ≈1.0 nm.[17] As shown in Figure 1f, with increased concentration from 1.0 to 5.0 M, there is a clear intensity increase in the q range from 0.5 to 0.8 $Å^{-1}$ (corresponding to a size of ≈7.8 Å), which can be ascribed to the formation of AGG clusters. The phenomena we observed in the concentrated siloxane electrolytes are similar to the results in other concentrated electrolytes.[10,18] As a result, significantly decreased solvent activity can be expected, which can benefit the suppression of LiPSs shuttle and lithium dendrite formation. However, these assumptions fail to consider the interaction between the coordinated solvents and charge/discharge intermediates/products, which are LiPSs in the case of Li–S batteries. To confirm the SIE process, we used Gaussian simulation to calculate the solvation energies of the cations/anions (Tables S2 to S4, Supporting Information) as well as the Gibbs free energy (ΔG) of the SIE in different solvents (Figure 1g and Table S5, Supporting Information). For the conventional ether solvents, the ΔG values are all negative for Li_2S_8, Li_2S_6, and Li_2S_4, indicating that SIE could occur in the DOL and DME systems spontaneously. On the contrary, the ΔG values for the siloxane are all positive, indicating the SIE reaction is highly unfavorable.

2.2. Tailoring Sulfur Redox Chemistry

To confirm the effect of SIE on the electrochemistry of sulfur cathodes, we have used a highly porous carbon (denoted as HPC1) with a pore size of ≈33 nm (Figure S6a, Supporting Information) to synthesize a S/HPC1 composite with a sulfur

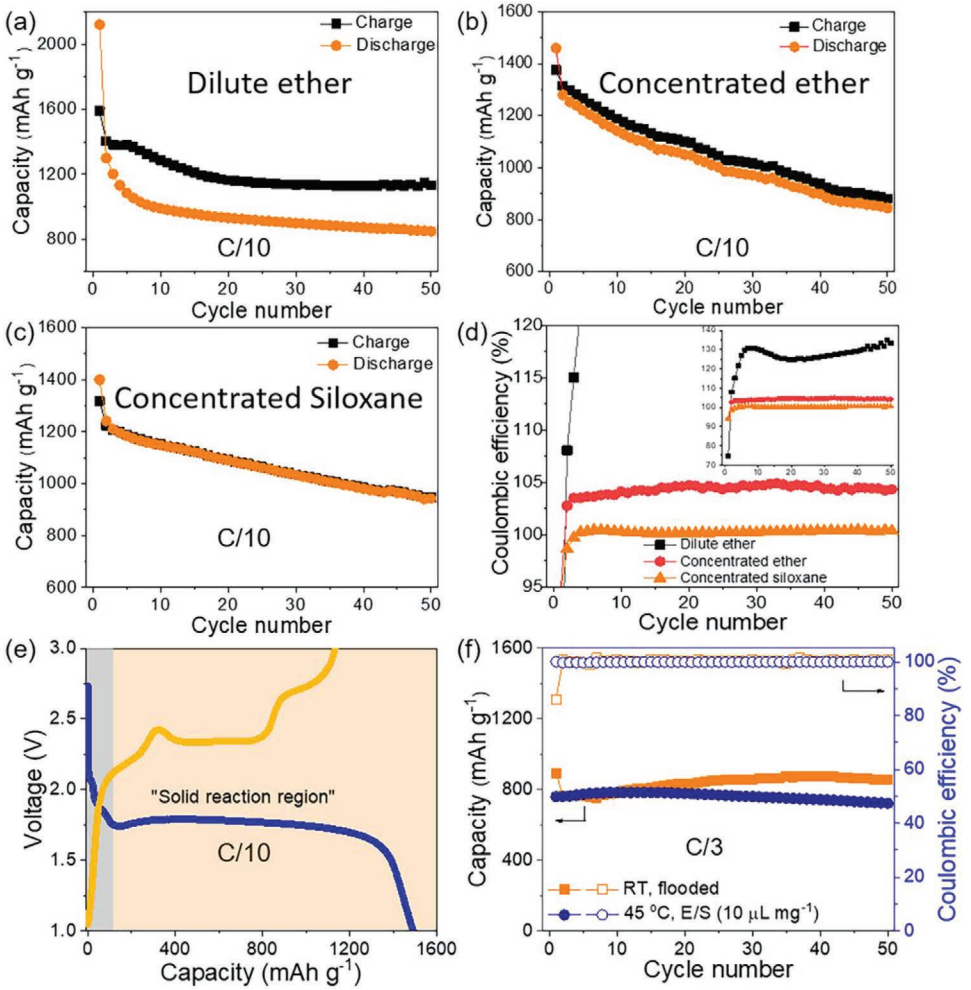

Figure 2. Cycle performance of S/HPC1 cathode in different electrolytes at C/10: a) dilute ether, b) concentrated ether, and c) concentrated siloxane. d) Comparison on the coulombic efficiency of S/HPC1 cathode in different electrolytes. e) First charge/discharge curve of S/HPC2 cathode in the concentrated siloxane electrolytes. f) Cycle performance of S/HPC2 cathode in the concentrated siloxane electrolytes at C/3 with flooded electrolytes and E/S ratio of 10 μL^{-1} mg^{-1}.

loading of 70 wt% (see the thermogravimetric analysis results in Figure S7, Supporting Information). This S/HPC1 composite can be deemed as a nonencapsulated sulfur cathode due to its relatively large pore size and can hence exclude the effect of sulfur confinement.

Figure 2a–c shows the cycle performance of the S/HPC1 cathode in the conventional dilute ether (DDL), concentrated ether (5DD), and concentrated siloxane (5DS) electrolytes (see the Experimental Section for details on the compositions of these electrolytes). Figure 2a shows the cycle performance of the S/HPC1 cathode in the conventional DDL electrolyte, indicating significant capacity fading and a severe shuttle effect during cycling of the S/HPC1 cathode. This poor performance is due to the weak confinement effect of HPC1, resulting in severe detachment of LiPSs from the cathode. In the 5DD electrolyte (Figure 2b), the shuttle effect was significantly suppressed compared to that for the DDL electrolyte. However, there are still obvious gaps between charge and discharge capacities, confirming the existence of a shuttle effect. By contrast, owing to the elimination of SIE in the 5DS electrolyte (Figure 2c), the S/HPC1 cathode did not show a visible shuttle effect. This can be seen more clearly in the coulombic efficiency comparison of Figure 2d. The cathode with 5DS electrolyte exhibits a superior coulombic efficiency of almost 100%, with ≈105% for 5DD and >120% for DDL, respectively. These results demonstrate that the 5DS electrolyte effectively eliminates the parasitic reactions. The length of CH_2CH_2O chain in the siloxane solvents will affect the ionic transport and conductivity of electrolytes.[19] Nevertheless, we found the concentrated siloxane electrolytes with longer CH_2CH_2O chain do not show visible shuttle effect as well (Figure S8, Supporting Information), representing a significant space for screening and optimization in the future.

We further investigated the synergistic effect of the 5DS electrolyte and sulfur confinement using a microporous carbon (HPC2) which has a pore size of ≈1–2 nm and a pore volume of 4.66 cc g^{-1} (Figure S6b, Supporting Information). With the same amount of sulfur loading (70 wt%), the S/HPC2 cathode exhibits a long discharge plateau in the 5DS electrolyte, corresponding to a quasi-solid-solid lithiation process, which is similar to results in our previous study using fluorinated ether

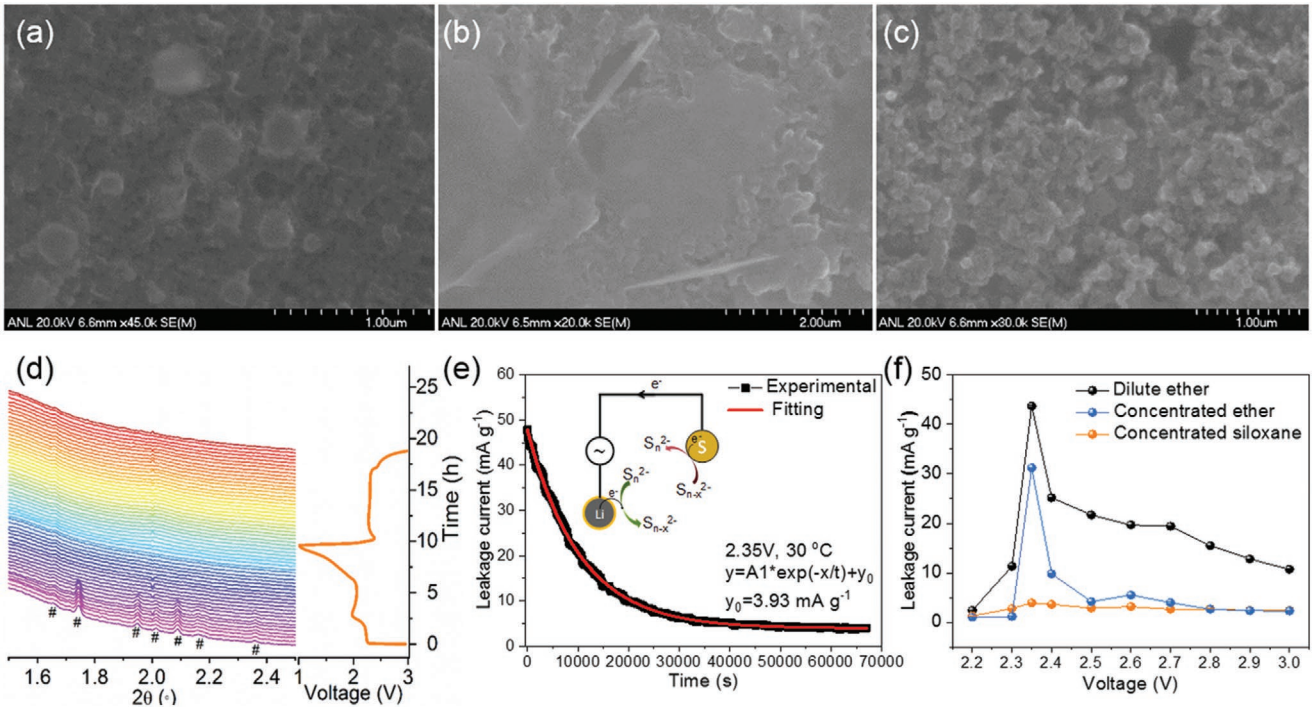

Figure 3. a) SEM images of cycled S/HPC1 cathode (20 cycles) in different electrolytes: a) dilute ether, b) concentrated ether, and c) concentrated siloxane-based electrolyte. d) In situ HEXRD measurements of S/HPC1 cathode in concentrated siloxane electrolyte. e) Scheme for the parasitic reactions inside Li/S battery during charge and the representative current relaxation curve collected to extract the static leakage current. f) Leakage current measurement of S/HPC1 cathode in different electrolytes.

electrolytes.[20] By contrast, the S/HPC2 cathode still exhibits two discharge voltage plateaus during lithiation in the DDL and 5DD electrolytes, corresponding to the conventional two-step solid–liquid–solid lithiation (Figure S9, Supporting Information). This result confirmed that the transformation of the lithiation pathway arises from the synergistic reaction between electrolytes and carbon structures. This is probably related to rational solid-electrolyte interphase distribution on different host structures, which thus prevent the contact between electrolytes solvents and electrode materials,[20,21] leading to the observed solid–solid lithiation/de-lithiation pathway. In addition, the S/HPC2 cathode present larger voltage polarization in the concentrated electrolytes than dilute electrolytes, which could be attributed to their large ionic transport resistance and viscosity as well as decreased polysulfides solubility.[22] Figure 2f displays the cycle performance of the S/HPC2 cathode with a flooded electrolyte at room temperature (RT) and with a low electrolyte-to-sulfur (E/S) ratio at 45 °C. Both conditions delivered stable cycle stability with high coulombic efficiency of around 100% at C/3 because of the bypassed formation of LiPSs and no SIE in the 5DS electrolyte, leading to almost no parasitic reactions. Noted that the S loading in the concentrated electrolytes is limited to 2 mg cm^{-2} due to their higher viscosity than dilute electrolytes. In order to enable high S loading electrodes (e.g., >5 mg cm^{-2}), searching for optimal diluents such as fluorinated ether to form localized concentrated electrolytes to enable high areal capacity for Li–S batteries is required and under investigation.[18b]

To further confirm the critical impact of the SIE process, we characterized the morphologies and structures of the S/HPC1 cathode by scanning electron microscopy (SEM) after testing in different electrolytes for 20 cycles. As shown in **Figure 3**a, there is obvious Li_2S/Li_2S_2 particle deposition outside the surface of the HPC1 cathode in the DDL electrolyte due to high dissolution of LiPSs and weak sulfur confinement effectiveness. In the case of 5DD electrolyte, it forms a film-like passivation layer on the cathode surface (Figure 3b), which is highly insulating and would block charge transfer across the sulfur/electrolyte interface and decrease the capacity during cycling.[12,18b] These results are both in contrast to that for the 5DS electrolyte cathode, which remained a highly porous structure similar to a pristine cathode (Figure 3c).

In situ high-energy X-ray diffraction (HEXRD) was conducted to track the phase transformation of S/HPC1 cathode during charge/discharge in the 5DS electrolyte. As shown in Figure 3d, the diffraction peaks marked by the # symbol in the pristine S/HPC1 cathode belong to crystalline S_8. During discharge, these peaks gradually disappear due to the reduction of S_8. However, in contrast to the results reported by Villevieille and co-workers,[23] we did not observe the LiPSs diffraction peaks during the whole discharge process, indicating no formation of soluble LiPSs. Furthermore, at the end of first discharge, no peaks corresponding to Li_2S were detected, indicating the Li_2S may be in a nanocrystalline form. During the charge process, we did not observe the re-formation of crystalline S_8. This finding is consistent with the SEM result, where no crystalline S_8 deposition or film-like products were seen.

To directly probe the parasitic reactions inside Li–S cells, we used a home-built system for high-precision leakage current measurement.[24] The working principle is illustrated in the

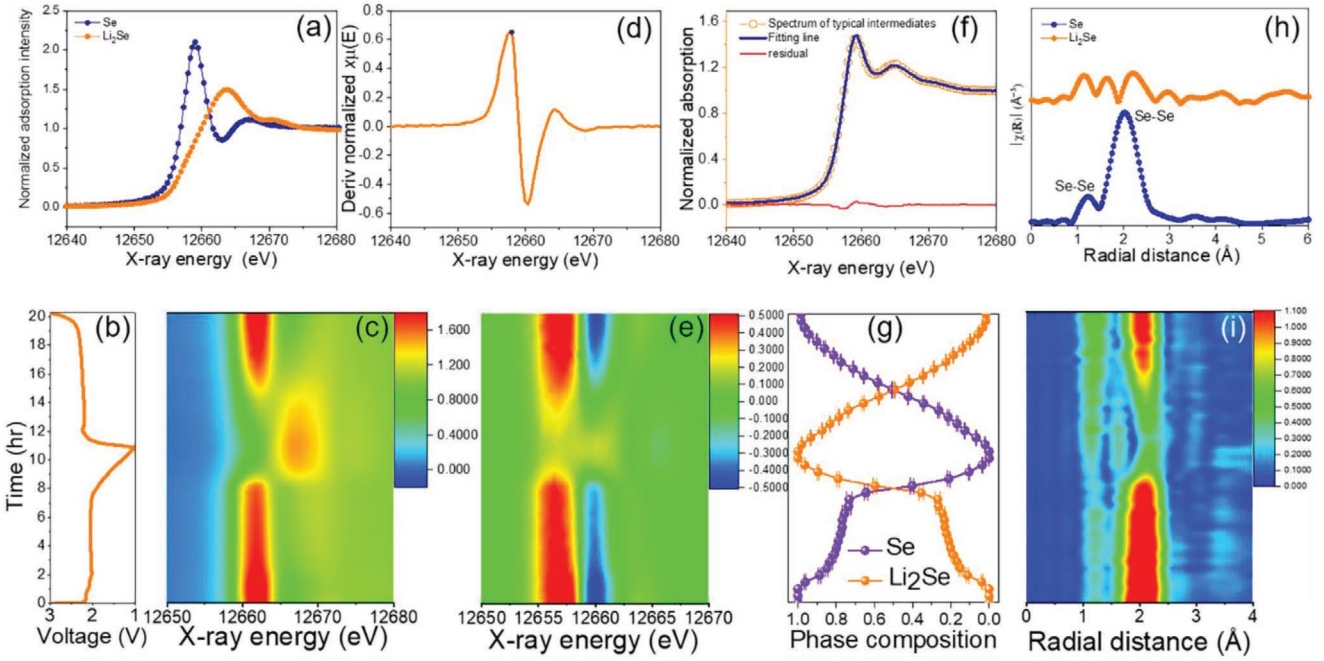

Figure 4. In situ Se K-edge XAFS results of Se/HPC1 cathode during charge/discharge at C/10 in the concentrated siloxane electrolyte: a) Normalized Se XANES spectra of standard Se and Li_2Se. b) Charge/discharge curve of Se/HPC1 cathode and c) corresponding 2D contour plot of in situ Se K-edge XANES. Derivative of normalized XANES spectra d) before and e) during the whole charge/discharge. f) Representative linear combination fitting of charge/discharge intermediates with two components (Se-Li_2Se). g) Relative composition of possible phases during charge/discharge. h) Spectra for EXAFS Se K-edge data of Se and Li_2Se. i) 2D contour plot of in situ EXAFS Se K-edge data.

Figure 3e inset. For this study, the Li–S cells were charged/discharged for two cycles and then charged at different constant voltage for 20 h. During this process, the long-chain LiPSs are chemically reduced by Li metal to form short-chain LiPSs at the anode side, while the short-chain LiPSs migrate to the cathode side and are electrochemically oxidized back to long-chain LiPSs. In this case, the number of electrons passing through the working electrode is directly proportional to the rate of parasitic reactions inside the Li–S cell (i.e., electrochemical oxidation of migrated short-chain LiPSs). As a result, the static leakage current can serve as a quantitative indicator for the parasitic reaction level, which can be extracted from the current relaxation curve by using the exponential decay function in Figure 3e. As clearly shown in Figure 3f, the leakage current is in the order of DDL > 5DD ≫ 5DS, further confirming the minimal parasitic reactions in the 5DS electrolyte due to the elimination of the SIE process.

To unravel the effect of the eliminated SIE on the lithiation pathway of the sulfur cathodes, we conducted a characterization study with operando synchrotron X-ray absorption spectroscopy (XAS). Unlike HEXRD, XAS can be used to investigate atoms of all states of matter, including solid, liquid, and crystalline and/or amorphous.[9c,25] In particular, X-ray absorption near edge spectroscopy (XANES) is very sensitive to the oxidation states of the targeted elements. Due to the interference of the sulfur signal from the LiTFSI in the electrolytes and the similarity between selenium and sulfur, we conducted in situ XAS Se K-edge characterization on the Se/HPC1 (70 wt% Se) cathode instead of S/HPC1 to elucidate the lithiation pathway.

Figure 4a shows the Se K-edge XANES curves of commercial Se and synthesized Li_2Se powder. Selenium powder exhibited an absorption energy of 12 658 eV due to the transition of Se 1s core electrons to the unoccupied 4p states, while the Se K-edge of Li_2Se moves to a higher energy of 12 664 eV.[25] Figure 4b,c shows the charge/discharge curves of the Se/HPC1 cathode in the 5DS electrolyte at C/10 along with the 2D contour plot from the in situ Se K-edge XANES. The features of Se remained almost constant during the long voltage plateau (≈8.0 h), and then Li_2Se started to dominate the discharge products due to the substantial generation of Li_2Se from Se. During the charge process, the Se signal is completely recovered, indicating high lithiation/de-lithiation reversibility. Figure 4d shows the first derivative of the XANES spectrum for commercial Se powder, from which the energy position of the edge can be determined. According to our previous work,[25] the energy shift of this peak is an indicator of LiPSs formation. However, as shown in Figure 4e, we do not observe a clear edge shift throughout the whole charge/discharge process, which is different from our previous results with dilute DOL/DME electrolytes.[25] To further confirm no formation of LiPSs, linear combination fitting was used for the XANES spectra during charge/discharge, which can determine the composition of the electrodes at different charge/discharge states. Figure 4f shows a typical fitting result using a two-phase (Se-Li_2Se) transition mode and reveals that the intermediates can be well fit to the data with minimum residue. The relative composition of Se and Li_2Se at different charge/discharge states, shown in Figure 4g, indicates a gradual decrease of Se along with an increase of Li_2Se during discharge. This process is reversed during the charge.

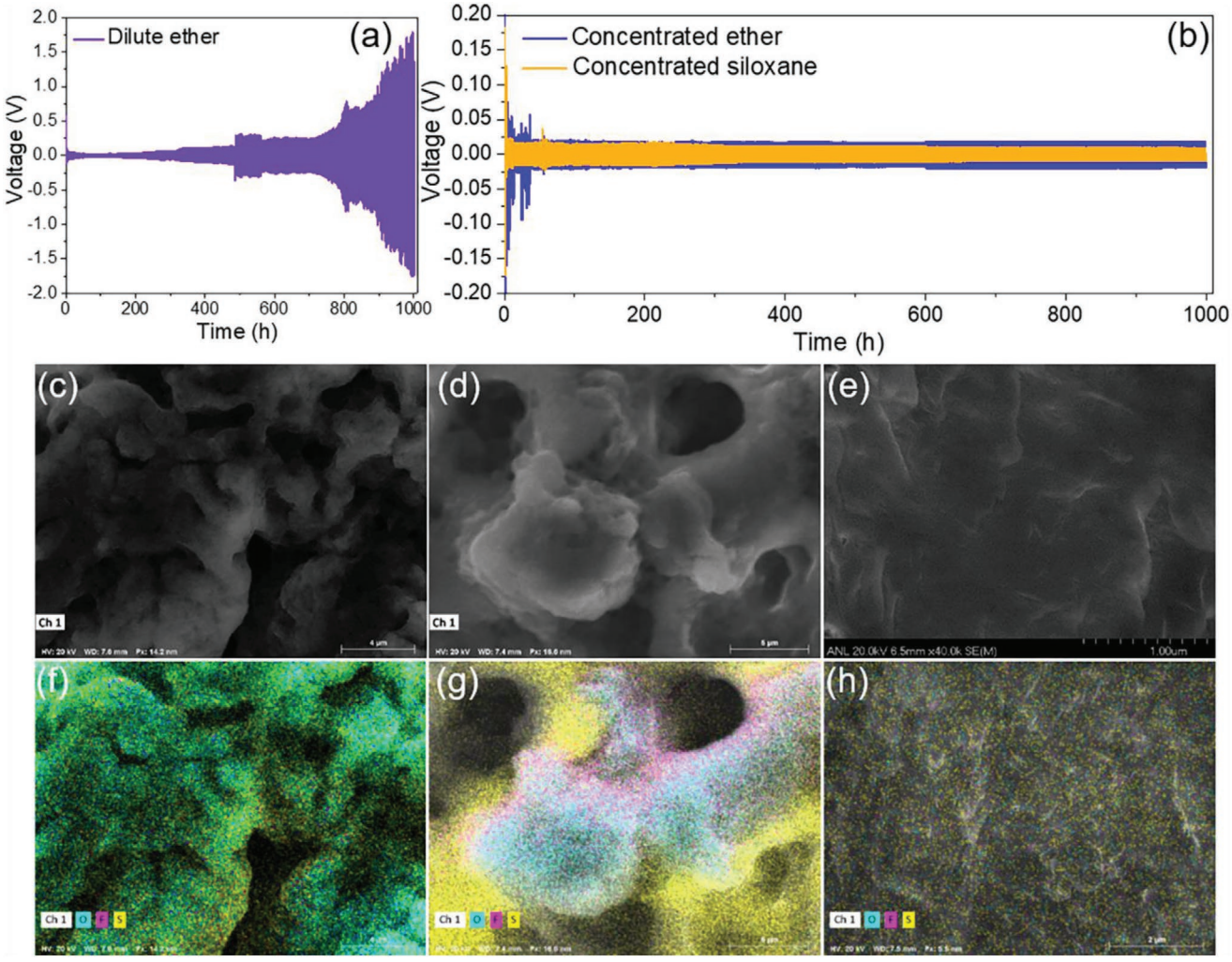

Figure 5. Li metal plating/stripping for Li/Li symmetric cells in a) dilute ether and b) concentrated electrolytes at 1.25 mA cm^{-2} with an areal capacity of 1.25 mAh cm^{-2}. SEM image of Li metal and corresponding EDX mapping in different electrolytes: c,f) dilute ether, d,g) concentrated ether, and e,h) concentrated siloxane electrolytes.

Compared to XANES, extended X-ray absorption fine structure (EXAFS) can probe the local electronic and bond structures of specific elements, and can thereby better visualize the structure changes during charge and discharge. The EXAFS spectra of Se and Li_2Se shown in Figure 4h exhibit significantly different features, which can be used to investigate the composition change. As clearly shown in Figure 4i and Figure S10 (Supporting Information), the electrode followed a direct transformation of Se to Li_2Se during discharge since there is no evolution of other peaks. The above XAS results confirm that the 5DS electrolyte can invoke a quasi-solid-solid lithiation pathway, which is one of the origins for the superior coulombic efficiency of the aforementioned Li–S cells due to elimination of the shuttle effect.

2.3. Li Plating/Stripping Stability and SEI Chemistries

In addition to the critical impact on the (de)lithiation mechanism of sulfur redox chemistry, the electrolytes also significantly altered the plating and stripping behavior of Li metal. **Figure 5**a,b compares the voltage profiles of Li/Li symmetric cells in different electrolytes for a 1000 h test period with a fixed areal capacity of 1.25 mAh cm^{-2} at 1.25 mA cm^{-2}. As expected, the DDL electrolyte exhibited a significant voltage polarization after only 200 h, while both 5DD and 5DS electrolytes exhibited stable voltage profiles during 1000 h of plating/stripping. This is because of the significantly suppressed free solvents in the concentrated electrolytes, while the significant amount of free solvents in the dilute electrolyte can induce severe parasitic reactions with Li metal. Note that the voltage polarization in the 5DS electrolyte is smaller than that in the 5DD electrolyte, which can be seen more clearly in Figure S11 (Supporting Information). This is probably related to their Li deposition process and thickness, which indicates that the 5DS may help form uniform and thinner Li. Subsequently, we found that the 5DS electrolyte can further maintain durable Li plating/stripping up to 2000 h (Figure S12, Supporting Information). The slight decrease of overpotential during repeated Li stripping/plating test in the concentrated siloxane electrolytes

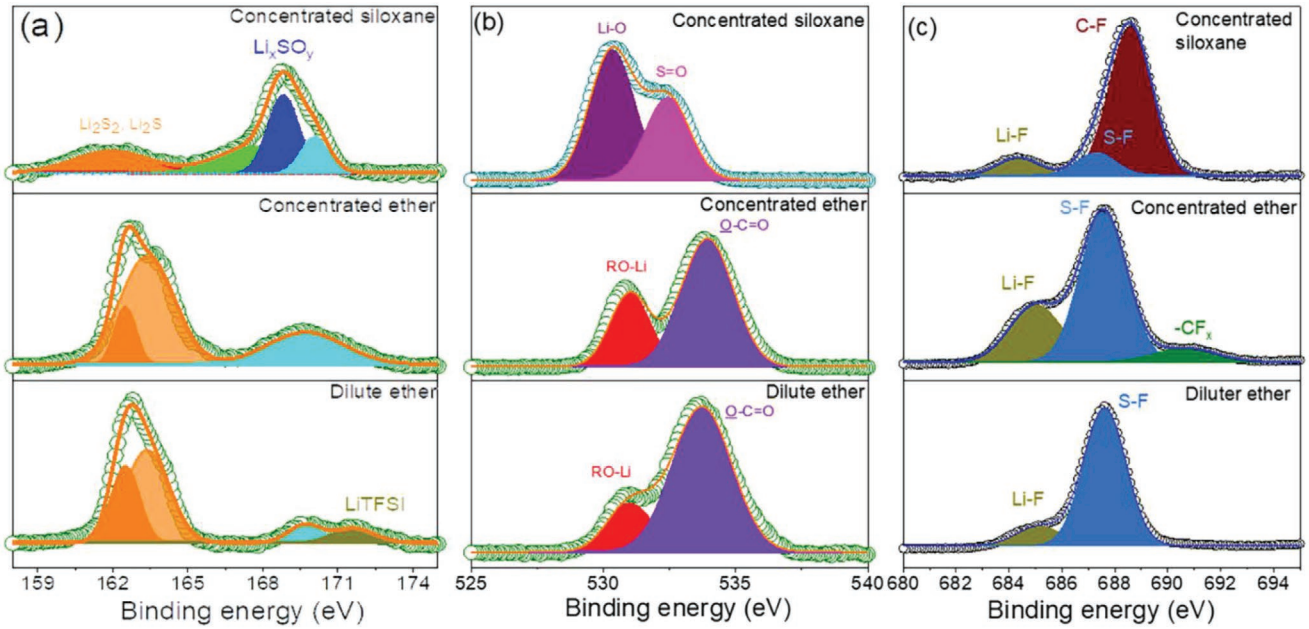

Figure 6. a) S 2p spectra, b) O 1s spectra, and c) F 1s spectra of Li metal in the Li/S-HPC1 cells after 20 cycles in different electrolytes at C/10.

was also reported in other modified electrolytes.[26] This could be due to the slight increase of Li metal surface area after repeated Li stripping/plating process, which thus decrease the true current densities of Li plating/stripping, and thus lead to the decrease of overpotential with cycling. The excellent Li plating/stripping behavior in the concentrated siloxane electrolyte has enabled its application in other high-energy electrode materials. Figure S13 (Supporting Information) shows the stable cycling performance of an amorphous silicon anode and a Ni-rich $LiNi_{0.6}Mn_{0.2}Mn_{0.2}O_2$ cathode in the 5DS electrolyte. Although the formulas for concentrated siloxane electrolytes to be used with different battery materials are under optimization, this result serves as a good proof-of-concept demonstrating the great application potential of the electrolytes in many electrode materials across a wide voltage window.

The results from the Li/Li symmetric cells are based on the suppressed solvent activities, but do not consider the effect of the aforementioned SIE. In the practical Li–S cells, the generation of LiPSs will definitely change the morphologies and structures of the Li metal and, hence, alter the Li plating/stripping behavior. The SEM images in Figure 5c–e show the morphologies of a cycled Li anode in Li–S/HPC1 cells after charge/discharge in different electrolytes for 20 cycles. As clearly shown, the cycled Li metal in DDL and 5DD electrolytes exhibited severe cracking and porous structures. On the contrary, the surface of the cycled Li metal in the 5DS electrolyte remained relatively flat. The energy-dispersive X-ray spectroscopy (EDX) mapping further confirmed a significant amount of Li_2S_x deposition on the surface of cycled Li metal in both dilute and concentrated ether electrolytes (Figure 5f,g), while only a small amount of F and S due to the formation of SEI can be observed in the concentrated siloxane electrolytes (Figure 5h). These differences in the morphologies and composition of the cycled Li anode between concentrated ether and concentrated siloxane electrolytes clearly confirm the effect of SIE in Li–S batteries.

We further characterized the cycled Li metal by X-ray photoelectron spectroscopy (XPS) to understand the compositional/structural characteristics of the SEI in different electrolytes and the related ionic transport across the interface. **Figure 6**a shows the S2p spectra of cycled Li metal after charge/discharge in different electrolytes for 20 cycles. The peaks at 159–165 eV belong to the deposition of Li_2S_2-Li_2S, and the peaks at 168–171 eV can be generally assigned to the formation of Li_xSO_y due to the reduction of LiTFSI in the SEI.[27] In contrast to the XPS S2p results of concentrated ether electrolytes obtained by Yushin and co-workers,[28] the abnormally high intensity of Li_2S_2-Li_2S clearly indicates a significant amount of Li_2S_2-Li_2S deposition on the cycled Li metal in the DDL and 5DD electrolytes, while almost no Li_2S_2-Li_2S deposition can be found in the case of 5DS electrolyte. This occurs because of the synergistic effect of suppressed solvent activities and eliminated SIE in the concentrated siloxane electrolyte. In 5DD electrolyte, however, the regeneration of free solvents through the SIE process would still lead to formation of LiPSs and further corrosion of Li metal. This can be further confirmed by the O1s and F1s spectra result. Two peaks corresponding to RO-Li (≈531 eV) and surface O—C=O (≈533.6 eV) can be observed in spectra for the DDL and 5DD electrolytes (Figure 6b), which are attributed to the reduction of ether solvents during cycling.[29] However, these peaks disappeared in the case of 5DS electrolyte (Figure 6b). Instead, two peaks due to the reduction of LiTFSI appeared at ≈530.3 eV (Li–O) and ≈532.5 eV (S=O), respectively. The decomposition of siloxane and DOL solvent did not participate the formation of SEI, which can be confirmed by the absence of Si–O (533.0 eV) and O—C=O (≈533.6 eV). The F1s spectrum of DDL exhibited two peaks at around 685 and 687.5 eV, which can be assigned to Li–F and S–F from decomposition of LiTFSI (Figure 6c). By increasing the concentration of LiTFSI, we found that the reduction of LiTFSI was enhanced in the 5DD electrolyte. When switching to concentrated siloxane electrolyte, the

spectra exhibited a C–F peak at the highest intensity and minor components of Li–F and S–F, similar to the SEI composition derived from dual-salt ether electrolytes.[27] As indicated by Xu and co-workers, these larger anion fragments such as the C–F moiety will be further reduced during cycling, leading to more LiF formation and stable cycle life in $Li/LiNi_{0.6}Mn_{0.2}Mn_{0.2}O_2$ and $Cu/LiNi_{0.6}Mn_{0.2}Mn_{0.2}O_2$ cells. Therefore, the concentrated siloxane electrolyte could enable an ultralong Li plating/stripping, as shown in Figure S12 (Supporting Information).

2.4. Intrinsic Nonflammability

Ether electrolytes are highly flammable due to their low flash points, which raise serious safety concern for large-scale batteries. As shown in Video S1 and Figure S14 (Supporting Information), the dilute ether electrolytes can ignite after only one ignition, demonstrating extremely high flammability. Concentrated ether electrolytes are more resistant to burning, but still flammable. Interestingly, the concentrated siloxane electrolyte is intrinsically nonflammable. It could not be ignited during the flammability test. Therefore, it could remarkably improve the safety performance of lithium metal batteries.

3. Conclusion

We have developed a new class of concentrated siloxane-based electrolyte for long-life and safe lithium–metal batteries, which demonstrate significant improvements over the widely used ether-based electrolyte in terms of electrochemical performance and flammability. Through a series of experimental and computational studies, we have elucidated the critical role of the hidden SIE process in Li–S batteries, which originates from the solvating power difference of cations/anions (i.e., Li^+, $TFSI^-$, S_x^{2-}, and FSI^-) with the solvents. By regulating the SIE, the concentrated siloxane electrolyte can not only effectively eliminate the shuttle effect through tailoring the transformation pathway of sulfur cathode, but also enable durable Li plating/stripping for Li metal, leading to almost no parasitic reactions for Li–S batteries. Future electrolyte design to improve the performance of practical Li–S batteries should consider the effect of salt anions and solvents on the SIE process.

4. Experimental Section

Preparation of Highly Porous Carbon (HPC) and S/HPC Composites: For the synthesis of the HPC1 material with large pore size, a modified parameter that was previously reported was used,[30] in which the weight ratio of silica to sucrose was changed to 1/1. The HPC2 activated carbon was prepared using starch sourced from corn (Sigma–Aldrich) as a carbon precursor. The activation process was proceeded by pyrolysis of starch at 650 °C in nitrogen atmosphere. The process was carried out by 1 h with carbon yield of 18%. In the next step, the chemical activation was carried out in an inert atmosphere (nitrogen flow) at 800 °C, with the C:KOH ratio of 1:4. After the entire process, obtained carbon was washed several times to remove the residue of the activator. The carbon yield after activation process was ≈60%

S/HPC1 and S/HPC2 composites with a sulfur loading of 70 wt% were prepared by mixing sulfur powder and HPC powder in a weight ratio of 7/3. The powders were then sealed in a hydrothermal vessel under argon. The sealed vessel was heated to 155 °C for 12 h in an oven before being cooled to room temperature naturally. A Se/HPC1 composite with a selenium loading of 70 wt% was also prepared under a similar process but with a high heating temperature of 260 °C.

Electrochemical Characterization: The S/HPC laminates were prepared by spreading a mixture of 70 wt% S/HPC composites, 20 wt% Super P, and 10 wt% PVDF (8.0 wt% in NMP) onto an aluminum foil current collector. The as-prepared electrodes were then dried at 55 °C in a vacuum oven overnight. The loading density of the active materials in the S/HPC electrodes was controlled at about 1.5–2.0 mg cm^{-2}. The electrochemical performance of the S/HPC electrodes was evaluated by assembling them into coin cells (type CR2032) in an argon-filled glovebox with moisture and oxygen content both below 1.0 ppm. The electrode was separated from a lithium counterelectrode by a separator (glass fiber, Grade GF/F Glass Microfiber Filter Binder Free, circle, 125 mm).

The DDL electrolyte was composed of 1.0 M lithium bis(trifluoromethanesulfonyl)imide (LiTFSI) in 1,3-dioxolane (DOL) and 1,2-dimethoxyethane (DME) (1/1 volume ratio) with 0.1 M $LiNO_3$ additive. The 5DD electrolyte was composed of 5.0 M LiTFSI in the DOL and DME (1/1, v/v). The 5DS electrolyte was composed of 5.0 M LiTFSI in DOL and 2,2-dimethyl-3,6,9-trioxa-2-siladecane (1/1 volume ratio). The assembled cells were tested with a MACCOR cycler or LAND cycler in the voltage range 1.0–3.0 V.

A parasitic reaction study was conducted in a home-built system with high-precision leakage current measurement.[24] A Li plating/stripping experiment was conducted with Li/Li symmetric cells using different electrolytes having a fix areal capacity of 1.25 mAh cm^{-2}. The cells were tested at 1.25 mA cm^{-2}.

Materials Characterization: The morphologies and structures of the materials were characterized by field emission scanning electron microscopy (HITACHI S-4700-II). The sulfur content in the S/HPC1 composite was measured by thermo-gravimetric analyses on a STA 449 F3 instrument under an argon atmosphere. The surface area, porosity, and pore size were determined in a gas sorption system (QUANTACHROME AUTOSORB 6-B). The samples were degassed at 110 °C for at least 20 h under vacuum, and then nitrogen adsorption/desorption isotherms were obtained at a constant temperature of 77.4 K. The various textural properties were all determined from the isotherms. The specific surface area was calculated by the Brunauer–Emmett–Teller method (seven points). The pore volume was estimated from single-point adsorption at a targeted relative pressure of 0.995. The pore size distribution was determined from the adsorption branch, according to the Barrett–Joyner–Halanda method. X-ray photoelectron spectroscopy analyses on cycled Li metal were performed with a ESCALAB 250Xi system using a monochromatized Al K source and equipped with an Ar^+ ion sputtering gun (Thermo Fisher). The Raman spectra of different concentrations of siloxane electrolyte were obtained with a Renishaw inVia microscope spectrometer.

Solution SAXS experiments were performed at beamline 12-ID-B of the Advanced Photon Source (APS) at Argonne National Laboratory. The wavelength, λ, of X-ray radiation was set to 0.886 Å. Scattered X-ray intensities were measured simultaneously with two Pilatus detectors, i.e., Pilatus 2M and 300k. The detectors were set such that the overall detection range of momentum transfer q [$= 4\pi \sin\theta/\lambda$, where 2θ is the scattering angle] was 0.004–2.3 $Å^{-1}$. All solution samples were measured with a flow cell consisting of a cylindrical quartz capillary (1.5 mm in diameter and 10 µm wall thickness). The flow rate was set at 10 µL s^{-1}, and the exposure time was set to ≈1 s to reduce possible radiation damage. To obtain good signal-to-noise ratio values, 20 images were acquired for each sample. The 2D scattering images were converted to 1D scattering curves ($I(q)$ vs q) through azimuthal averaging after solid angle correction and then normalization with the intensity of the transmitted X-ray beam flux by means of beamline software. The two scattering curves for each sample collected from two detectors were eventually merged into one curve. An ignition and combustion experiment of different electrolytes was conducted by using the same

amount (1.0 mL) of electrolytes followed by immediate ignition with a butane lighter.

Operando HEXRD and Se K-Edge XANES Measurements: Coin cells with a hole on both the top and bottom case were used for the operando X-ray experiments. Operando synchrotron HEXRD experiments were carried out at Beamline 11-ID-C of the APS using X-rays with wavelengths of 0.1173 Å. Operando XANES experiments on the Se K-edge between 12 458 and 13 458 eV were carried out in transmission mode at Beamline 20-BM-B of the APS. The incident beam was monochromatized by using a Si(111) fixed-exit, double-crystal monochromator. During the operando experiment, a MACCOR cycler was used to charge/discharge the cells at a constant rate of C/10 (1 C = 675 mA g^{-1}) between 1.0 and 3.0 V.

Computational Details: All the calculations, including geometry optimizations, were performed with density functional theory (DFT) using the B3LYP functional with the 6–311G++(d,p) basis set. The solvation free energy was calculated from the difference in free energy of the solute in the solution and gas phase. The solvation model based on density (SMD) in GAUSSIAN 09 was chosen for computing the solvation free energy.

All electronic calculations were carried out using the Perdew–Burke–Ernzerhof functional of exchange correlation and the projector-augmented-wave pseudopotentials.[31] D3 dispersion corrections with zero damping were used to describe the van der Waals forces.[32] The cut-off energy was 350 eV, and a gamma Monkhorst-Pack k-point sampling was used. A mixed solution placed in a cubic box was assumed with a length of 17 Å containing 7 siloxane ($C_8H_{20}O_3Si$) molecules and 21 DOL ($C_3H_6O_2$) molecules with the volume ratio being 1.02, which is close to 1 in experiments. By adding 3, 6, 9, 12, and 15 LiTFSI ($C_2F_8LiNO_4S_2$) molecules into the mixed solution, one can continuously control the Li^+ concentration from 1 to 5 M. For each concentration, 10 ps (1 fs per step) AIMD simulations were performed to rapidly equilibrate the system at first within the canonical (NVT) ensemble at 600 K. The molecular dynamics simulation was run for 10 ps at 300 K to collect the structures around the Li^+ center. The coordination number of Li^+ was obtained by averaging 20 samples taken from the last 5 ps of molecular dynamics simulations.

Supporting Information

Supporting Information is available from the Wiley Online Library or from the author.

Acknowledgements

R.A. and J.L. contributed equally to this work. Research at the Argonne National Laboratory was funded by the U.S. Department of Energy (DOE), Vehicle Technologies Office. Support from Tien Duong of the U.S. DOE's Office of Vehicle Technologies Program is gratefully acknowledged. Use of the Advanced Photon Source (APS), an Office of Science User Facility operated for the DOE Office of Science by Argonne National Laboratory, was supported by DOE under Contract No. DE-AC02-06CH11357. The authors also acknowledge the support from National Natural Science Foundation of China (21903001) and Natural Science Foundation of Anhui Province (1908085QB58) for the AIMD simulation. Saudi contribution was funded by the University of Jeddah, Saudi Arabia, under grant no. (UJ-07-18-ICP). K.F. acknowledges the European Commission and the European Research Council for financial support within the Starting Grant project (GA 759603) under the European Union's Horizon 2020 Research and Innovation Programme. I.A. and K.L. acknowledge the financial support from the Polish Ministry of Science and Education -Grant No 3787/E-138/S/2017. An error in the legend of Figure 3f was fixed on July 7, 2020.

Conflict of Interest

The authors declare no conflict of interest.

Keywords

concentrated electrolytes, lithium metal batteries, siloxanes, solvation-ion-exchange, sulfur

Received: March 9, 2020
Revised: April 22, 2020
Published online: June 2, 2020

[1] a) Z. W. Seh, Y. M. Sun, Q. F. Zhang, Y. Cui, *Chem. Soc. Rev.* **2016**, *45*, 5605; b) X. Yang, X. Li, K. Adair, H. Zhang, X. Sun, *Electrochem. Energy Rev.* **2018**, *1*, 239.

[2] a) A. Manthiram, Y. Fu, S.-H. Chung, C. Zu, Y.-S. Su, *Chem. Rev.* **2014**, *114*, 11751; b) C. Huang, J. Xiao, Y. Shao, J. Zheng, W. D. Bennett, D. Lu, L. V. Saraf, M. Engelhard, L. Ji, J. Zhang, X. Li, G. L. Graff, J. Liu, *Nat. Commun.* **2014**, *5*, 3015.

[3] P. P. R. M. L. Harks, C. B. Robledo, T. W. Verhallen, P. H. L. Notten, F. M. Mulder, *Adv. Energy Mater.* **2017**, *7*, 1601635.

[4] a) R. G. Cao, W. Xu, D. P. Lv, J. Xiao, J. G. Zhang, *Adv. Energy Mater.* **2015**, *5*, 3059; b) D. Lin, Y. Liu, Y. Cui, *Nat. Nanotechnol.* **2017**, *12*, 194.

[5] a) Q. Pang, X. Liang, C. Y. Kwok, L. F. Nazar, *Nat. Energy* **2016**, *1*, 16132; b) X. Yang, X. Gao, Q. Sun, S. P. Jand, Y. Yu, Y. Zhao, X. Li, K. Adair, L. Y. Kuo, J. Rohrer, J. Liang, X. Lin, M. N. Banis, Y. Hu, H. Zhang, X. Li, R. Li, H. Zhang, P. Kaghazchi, T.-K. Sham, X. Sun, *Adv. Mater.* **2019**, *31*, 1901220.

[6] X. Ji, K. T. Lee, L. F. Nazar, *Nat. Mater.* **2009**, *8*, 500.

[7] S. Evers, L. F. Nazar, *Acc. Chem. Res.* **2013**, *46*, 1135.

[8] a) B. He, W. C. Li, C. Yang, S. Q. Wang, A. H. Lu, *ACS Nano* **2016**, *10*, 1633; b) Z. A. Ghazi, L. Y. Zhu, H. Wang, A. Naeem, A. M. Khattak, B. Liang, N. A. Khan, Z. X. Wei, L. S. Li, Z. Y. Tang, *Adv. Energy Mater.* **2016**, *6*, 1601250; c) J. X. Song, M. L. Gordin, T. Xu, S. R. Chen, Z. X. Yu, H. Sohn, J. Lu, Y. Ren, Y. H. Duan, D. H. Wang, *Angew. Chem., Int. Ed.* **2015**, *54*, 4325.

[9] a) S. Zhang, K. Ueno, K. Dokko, M. Watanabe, *Adv. Energy Mater.* **2015**, *5*, 1500117; b) G.-L. Xu, J. Liu, R. Amine, Z. Chen, K. Amine, *ACS Energy Lett.* **2017**, *2*, 605; c) G.-L. Xu, T. Ma, C.-J. Sun, C. Luo, L. Cheng, Y. Ren, S. M. Heald, C. Wang, L. Curtiss, J. Wen, D. J. Miller, T. Li, X. Zuo, V. Petkov, Z. Chen, K. Amine, *Nano Lett.* **2016**, *16*, 2663.

[10] J. Qian, W. A. Henderson, W. Xu, P. Bhattacharya, M. Engelhard, O. Borodin, J.-G. Zhang, *Nat. Commun.* **2015**, *6*, 6362.

[11] S. Hess, M. Wohlfahrt-Mehrens, M. Wachtler, *J. Electrochem. Soc.* **2015**, *162*, A3084.

[12] H. Pan, J. Chen, R. Cao, V. Murugesan, N. N. Rajput, K. S. Han, K. Persson, L. Estevez, M. H. Engelhard, J.-G. Zhang, K. T. Mueller, Y. Cui, Y. Shao, J. Liu, *Nat. Energy* **2017**, *2*, 813.

[13] H. Chu, H. Noh, Y.-J. Kim, S. Yuk, J.-H. Lee, J. Lee, H. Kwack, Y. Kim, D.-K. Yang, H.-T. Kim, *Nat. Commun.* **2019**, *10*, 188.

[14] a) Y. Yamada, A. Yamada, *J. Electrochem. Soc.* **2015**, *162*, A2406; b) W.-J. Chen, B.-Q. Li, C.-X. Zhao, M. Zhao, T.-Q. Yuan, R.-C. Sun, J.-Q. Huang, Q. Zhang, *Angew. Chem., Int. Ed.* **2020**, *59*, 2.

[15] J. Zheng, J. A. Lochala, A. Kwok, Z. D. Deng, J. Xiao, *Adv. Sci.* **2017**, *4*, 1700032.

[16] a) L. Suo, Y.-S. Hu, H. Li, M. Armand, L. Chen, *Nat. Commun.* **2013**, *4*, 1481; b) Y. Z. Zhang, S. Liu, G. C. Li, G. R. Li, X. P. Gao, *J. Mater. Chem. A* **2014**, *2*, 4652.

[17] Z. Feng, E. Sarnello, T. Li, L. Cheng, *J. Electrochem. Soc.* **2019**, *166*, A47.

[18] a) J. Wang, Y. Yamada, K. Sodeyama, C. H. Chiang, Y. Tateyama, A. Yamada, *Nat. Commun.* **2016**, *7*, 12032; b) Q. Pang, A. Shyamsunder, B. Narayanan, C. Y. Kwok, L. A. Curtiss, L. F. Nazar, *Nat. Energy* **2018**, *3*, 783.

[19] Z. Chen, H. H. Wang, D. R. Vissers, L. Zhang, R. West, L. J. Lyons, K. Amine, *J. Phys. Chem. C* **2008**, *112*, 2210.
[20] G.-L. Xu, H. Sun, C. Luo, L. Estevez, M. Zhuang, H. Gao, R. Amine, H. Wang, X. Zhang, C.-J. Sun, Y. Liu, Y. Ren, S. M. Heald, C. Wang, Z. Chen, K. Amine, *Adv. Energy Mater.* **2019**, *9*, 1802235.
[21] H. Yang, C. Guo, J. Chen, A. Naveed, J. Yang, Y. Nuli, J. Wang, *Angew. Chem., Int. Ed.* **2019**, *58*, 791.
[22] A. Gupta, A. Bhargav, A. Manthiram, *Adv. Energy Mater.* **2019**, *9*, 1803096.
[23] J. Conder, R. Bouchet, S. Trabesinger, C. Marino, L. Gubler, C. Villevieille, *Nat. Energy* **2017**, *2*, 17069.
[24] X. Q. Zeng, G. L. Xu, Y. Li, X. Y. Luo, F. Maglia, C. Bauer, S. F. Lux, O. Paschos, S. J. Kim, P. Lamp, J. Lu, K. Amine, Z. H. Chen, *ACS Appl. Mater. Interfaces* **2016**, *8*, 3446.
[25] Y. Cui, A. Abouimrane, J. Lu, T. Bolin, Y. Ren, W. Weng, C. Sun, V. A. Maroni, S. M. Heald, K. Amine, *J. Am. Chem. Soc.* **2013**, *135*, 8047.
[26] a) S. Bai, Y. Sun, J. Yi, Y. He, Y. Qiao, H. Zhou, *Joule* **2018**, *2*, 2117; b) X.-B. Cheng, C. Yan, H.-J. Peng, J.-Q. Huang, S.-T. Yang, Q. Zhang, *Energy Storage Mater.* **2018**, *10*, 199.
[27] J. Alvarado, M. A. Schroeder, T. P. Pollard, X. F. Wang, J. Z. Lee, M. H. Zhang, T. Wynn, M. Ding, O. Borodin, Y. S. Meng, K. Xu, *Energy Environ. Sci.* **2019**, *12*, 780.
[28] H. Kim, F. Wu, J. T. Lee, N. Nitta, H.-T. Lin, M. Oschatz, W. I. Cho, S. Kaskel, O. Borodin, G. Yushin, *Adv. Energy Mater.* **2015**, *5*, 1401792.
[29] A. K. Chan, R. Tatara, S. Feng, P. Karayaylali, J. Lopez, I. E. L. Stephens, Y. Shao-Horn, *J. Electrochem. Soc.* **2019**, *166*, A1867.
[30] L. Estevez, R. Dua, N. Bhandari, A. Ramanujapuram, P. Wang, E. P. Giannelis, *Energy Environ. Sci.* **2013**, *6*, 1785.
[31] a) P. E. Blöchl, *Phys. Rev. B* **1994**, *50*, 17953; b) G. Kresse, J. Furthmüller, *Phys. Rev. B* **1996**, *54*, 11169; c) G. Kresse, J. Hafner, *Phys. Rev. B* **1993**, *47*, 558; d) J. P. Perdew, K. Burke, M. Ernzerhof, *Phys. Rev. Lett.* **1996**, *77*, 3865.
[32] S. Grimme, J. Antony, S. Ehrlich, H. Krieg, *J. Chem. Phys.* **2010**, *132*, 154104.